Spectral pulse transformations and phase transitions in quadratic nonlinear waveguide arrays

Frank Setzpfandt,[1,*] Andrey A. Sukhorukov,[2] Dragomir N. Neshev,[2] Roland Schiek,[3] Alexander S. Solntsev,[2] Raimund Ricken,[4] Yoohong Min,[4] Wolfgang Sohler,[4] Yuri S. Kivshar,[2] and Thomas Pertsch[1]

[1]*Institute of Applied Physics, Abbe Center of Photonics, Friedrich-Schiller-Universität Jena, Max-Wien-Platz 1, 07743 Jena, Germany*

[2]*Nonlinear Physics Centre, RSPE, Australian National University, Canberra, ACT 0200, Australia*

[3]*University of Applied Sciences Regensburg, Prüfeninger Strasse 58, 93049 Regensburg, Germany*

[4]*Applied Physics, University of Paderborn, Warburger Strasse 100, 33095 Paderborn, Germany*

[*]*f.setzpfandt@uni-jena.de*

Abstract: We study experimentally and numerically the dynamics of a recently found topological phase transition for discrete quadratic solitons with linearly coupled SH waves. We find that, although no stationary states are excited in the experimental situation, the generic feature of the phase transition of the SH is preserved. By utilizing simulations of the coupled mode equations we identify the complex processes leading to the phase transition involving spatial focusing and the generation of new frequency components. These distinct signatures of the dynamic phase transition are also demonstrated experimentally.

OCIS codes: (190.0190) Nonlinear optics; (190.4410) Nonlinear optics, parametric processes; (190.7110) Ultrafast nonlinear optics.

References and links

1. D. N. Christodoulides, F. Lederer, and Y. Silberberg, "Discretizing light behaviour in linear and nonlinear waveguide lattices," Nature **424**, 817–823 (2003).
2. A. Szameit and S. Nolte, "Discrete optics in femtosecond-laser-written photonic structures," J. Phys. B **43**, 163001 (2010).
3. H. S. Eisenberg, Y. Silberberg, R. Morandotti, and J. S. Aitchison, "Diffraction management," Phys. Rev. Lett. **85**, 1863–1866 (2000).
4. T. Pertsch, T. Zentgraf, U. Peschel, A. Bräuer, and F. Lederer, "Anomalous refraction and diffraction in discrete optical systems," Phys. Rev. Lett. **88**, 093901 (2002).
5. S. Longhi, "Quantum-optical analogies using photonic structures," Laser Photon. Rev. **3**, 243–261 (2009).
6. C. Denz, S. Flach, and Y. S. Kivshar, eds., *Nonlinearities in Periodic Structures and Metamaterials* (Springer, 2010).
7. A. B. Aceves, C. D. Angelis, S. Trillo, and S. Wabnitz, "Storage and steering of self-trapped discrete solitons in nonlinear waveguide arrays," Opt. Lett. **19**, 332–334 (1994).
8. O. Bang and P. D. Miller, "Exploiting discreteness for switching in waveguide arrays," Opt. Lett. **21**, 1105–1107 (1996).
9. R. A. Vicencio, M. I. Molina, and Y. S. Kivshar, "Controlled switching of discrete solitons in waveguide arrays," Opt. Lett. **28**, 1942–1944 (2003).

#153927 - $15.00 USD Received 7 Sep 2011; revised 16 Oct 2011; accepted 20 Oct 2011; published 1 Nov 2011

10. T. Pertsch, R. Iwanow, R. Schiek, G. I. Stegeman, U. Peschel, F. Lederer, Y. H. Min, and W. Sohler, "Spatial ultrafast switching and frequency conversion in lithium niobate waveguide arrays," Opt. Lett. **30**, 177–179 (2005).
11. F. Lederer, G. I. Stegeman, D. N. Christodoulides, G. Assanto, M. Segev, and Y. Silberberg, "Discrete solitons in optics," Phys. Rep. **463**, 1–126 (2008).
12. H. S. Eisenberg, Y. Silberberg, R. Morandotti, A. R. Boyd, and J. S. Aitchison, "Discrete spatial optical solitons in waveguide arrays," Phys. Rev. Lett. **81**, 3383–3386 (1998).
13. A. Szameit, J. Burghoff, T. Pertsch, S. Nolte, A. Tünnermann, and F. Lederer, "Two-dimensional soliton in cubic fs laser written waveguide arrays in fused silica," Opt. Express **14**, 6055–6062 (2006).
14. J. W. Fleischer, M. Segev, N. K. Efremidis, and D. N. Christodoulides, "Observation of two-dimensional discrete solitons in optically induced nonlinear photonic lattices," Nature **422**, 147–150 (2003).
15. R. Iwanow, R. Schiek, G. I. Stegeman, T. Pertsch, F. Lederer, Y. Min, and W. Sohler, "Observation of discrete quadratic solitons," Phys. Rev. Lett. **93**, 113902 (2004).
16. G. I. Stegeman, M. Sheik-Bahae, E. V. Stryland, and G. Assanto, "Large nonlinear phase shifts in second-order nonlinear-optical processes," Opt. Lett. **18**, 13–15 (1993).
17. R. Schiek, Y. Baek, and G. I. Stegeman, "Second-harmonic generation and cascaded nonlinearity in titanium-indiffused lithium niobate channel waveguides," J. Opt. Soc. Am. B **15**, 2255–2268 (1998).
18. F. Setzpfandt, A. A. Sukhorukov, D. N. Neshev, R. Schiek, Y. S. Kivshar, and T. Pertsch, "Phase transitions of nonlinear waves in quadratic waveguide arrays," Phys. Rev. Lett. **105**, 233905 (2010).
19. S. Droulias, K. Hizanidis, J. Meier, and D. Christodoulides, "X - waves in nonlinear normally dispersive waveguide arrays," Opt. Express **13**, 1827–1832 (2005).
20. Y. Lahini, E. Frumker, Y. Silberberg, S. Droulias, K. Hizanidis, R. Morandotti, and D. N. Christodoulides, "Discrete *x*-wave formation in nonlinear waveguide arrays," Phys. Rev. Lett. **98**, 023901 (2007).
21. M. Heinrich, A. Szameit, F. Dreisow, R. Keil, S. Minardi, T. Pertsch, S. Nolte, A. Tünnermann, and F. Lederer, "Observation of three-dimensional discrete-continuous *x* waves in photonic lattices," Phys. Rev. Lett. **103**, 113903 (2009).
22. S. Carrasco, J. P. Torres, D. Artigas, and L. Torner, "Generation of multicolor spatial solitons with pulsed light," Opt. Commun. **192**, 347–355 (2001).
23. F. Baronio, A. Barthelemy, S. Carrasco, V. Couderc, C. D. Angelis, L. Lefort, Y. Min, P. H. Pioger, V. Quiring, L. Torner, and W. Sohler, "Generation of quadratic spatially trapped beams with short pulsed light," J. Opt. B: Quantum Semiclassical Opt. **6**, S182–S189 (2004).
24. C. Conti and S. Trillo, "X waves generated at the second harmonic," Opt. Lett. **28**, 1251–1253 (2003).
25. O. Jedrkiewicz, J. Trull, G. Valiulis, A. Piskarskas, C. Conti, S. Trillo, and P. Di Trapani, "Nonlinear x waves in second-harmonic generation: Experimental results," Phys. Rev. E **68**, 026610 (2003).
26. G. Valiulis, V. Jukna, O. Jedrkiewicz, M. Clerici, E. Rubino, and P. DiTrapani, "Propagation dynamics and x-pulse formation in phase-mismatched second-harmonic generation," Phys. Rev. A **83**, 043834 (2011).
27. R. Iwanow, G. I. Stegeman, R. Schiek, T. Pertsch, F. Lederer, Y. Min, and W. Sohler, "Highly localized discrete quadratic solitons," Opt. Lett. **30**, 1033–1035 (2005).
28. W. Sohler, H. Hu, R. Ricken, V. Quiring, C. Vannahme, H. Herrmann, D. Büchter, S. Reza, W. Grundkötter, S. Orlov, H. Suche, R. Nouroozi, and Y. Min, "Integrated optical devices in lithium niobate," Opt. Photon. News **19**, 24–31 (2008).
29. C. G. Trevino-Palacios, G. I. Stegeman, M. P. D. Micheli, P. Baldi, S. Nouh, D. B. Ostrowsky, D. Delacourt, and M. Papuchon, "Intensity dependent mode competition in second harmonic generation in multimode waveguides," Appl. Phys. Lett. **67**, 170–172 (1995).
30. F. Setzpfandt, D. N. Neshev, R. Schiek, F. Lederer, A. Tünnermann, and T. Pertsch, "Competing nonlinearities in quadratic nonlinear waveguide arrays," Opt. Lett. **34**, 3589–3591 (2009).
31. F. Setzpfandt, A. Sukhorukov, and T. Pertsch, "Discrete quadratic solitons with competing second-harmonic components" (submitted to Phys. Rev. A).
32. T. Peschel, U. Peschel, and F. Lederer, "Discrete bright solitary waves in quadratically nonlinear media," Phys. Rev. E **57**, 1127–1133 (1998).
33. A. A. Sukhorukov, Y. S. Kivshar, O. Bang, and C. M. Soukoulis, "Parametric localized modes in quadratic nonlinear photonic structures," Phys. Rev. E **63**, 016615 (2000).
34. W. Press, S. Teukolsky, W. Vetterling, and B. Flannery, *Numerical Recipes in C*, 2nd ed. (Cambridge University Press, 1992).
35. M. Bache, O. Bang, B. B. Zhou, J. Moses, and F. W. Wise, "Optical cherenkov radiation in ultrafast cascaded second-harmonic generation," Phys. Rev. A **82**, 063806 (2010).
36. J. T. Manassah, "Effects of velocity dispersion on a generated second harmonic signal," Appl. Opt. **27**, 4365–4367 (1988).
37. L. D. Noordam, H. J. Bakker, M. P. de Boer, and H. B. van Linden van den Heuvell, "Second-harmonic generation of femtosecond pulses: observation of phase-mismatch effects," Opt. Lett. **15**, 1464–1466 (1990).
38. R. Schiek, R. Iwanow, T. Pertsch, G. I. Stegeman, G. Schreiber, and W. Sohler, "One-dimensional spatial soliton families in optimallyengineered quasi-phase-matched lithium niobate waveguides," Opt. Lett. **29**, 596–598 (2004).

#153927 - $15.00 USD Received 7 Sep 2011; revised 16 Oct 2011; accepted 20 Oct 2011; published 1 Nov 2011

39. S. Johnson and J. Joannopoulos, "Block-iterative frequency-domain methods for maxwell's equations in a planewave basis," Opt. Express **8**, 173–190 (2001).
40. F. Setzpfandt, D. N. Neshev, A. A. Sukhorukov, R. Schiek, R. Ricken, Y. Min, Y. S. Kivshar, W. Sohler, F. Lederer, A. Tünnermann, and T. Pertsch, "Nonlinear dynamics with higher-order modes in lithium niobate waveguide arrays," Appl. Phys. B: Lasers Opt. **104**, 487–493 (2011).
41. C. B. Clausen, O. Bang, and Y. S. Kivshar, "Spatial solitons and induced kerr effects in quasi-phase-matched quadratic media," Phys. Rev. Lett. **78**, 4749–4752 (1997).
42. A. Kobyakov, F. Lederer, O. Bang, and Y. S. Kivshar, "Nonlinear phase shift and all-optical switching in quasi-phase-matched quadratic media," Opt. Lett. **23**, 506–508 (1998).

1. Introduction

In the last years, discrete optical systems and especially waveguide arrays (WGAs) have been an active area of research in optics [1, 2]. Due to their tunable diffraction properties [3, 4], WGAs are also a very versatile system to explore fundamental questions [5]. Nonlinear WGAs open new possibilities for optical beam control [6]. Here applications like switching, storing and routing of optical signals [7–10] are mostly interesting for telecommunications. Series of studies in recent years were devoted to fundamental aspects of nonlinear beam propagation in WGAs, especially to the properties of discrete spatial solitons [11]. Solitons are localized stationary wave packets which can form if the optical nonlinearity cancels the diffraction of an optical beam. Spatial solitons have been predicted and experimentally verified in 1D and 2D in WGAs with Kerr-nonlinearity [12, 13] and photorefractive nonlinearity [14]. In one-dimensional WGAs with second order nonlinearity spatial solitons have been also observed [15]. In these quadratic systems, the nonlinear phase shifts are generated by the parametric interaction of a fundamental wave (FW) with its second harmonic (SH) [16]. Usually, WGAs are multimode at the SH wavelength [17]. This creates an additional degree of freedom in these systems since different SH modes with different properties can be employed to generate phase shifts. Recently it has been shown, that the strong spatial coupling of higher order SH modes enables new properties of the spatial solitons, namely a power dependent topological transition between different spatial profiles of the soliton [18].

To experimentally realize spatial solitons in quadratic waveguide arrays, high optical powers are necessary. These can be only achieved by the use of short optical pulses. For wide spatial solitons, the temporal effects induced by short pulses can be mostly neglected [15]. However, the impact of temporal reshaping becomes more pronounced for strongly localized beams. It was shown for WGAs in Kerr media that spatio-temporal coupling and reshaping may lead to the formation of X-waves [19–21] which are fundamentally different from spatial solitons. In media with second order nonlinearity the role of temporal effects for the excitation of spatial solitons has been discussed for bulk propagation [22, 23]. Moreover, analysis of the SH dynamics in beams propagating in $\chi^{(2)}$-material showed the excitation of X-waves at the SH wavelengths from an input FW beam [24–26]. In WGAs with quadratic nonlinearities, highly localized spatial solitons have been reported [27], but the influence of the pulsed beams has not been analyzed in detail. Since the soliton phase transition reported in [18] critically depends on the strong localization of the propagating beams, we expect that temporal effects will have a profound effect on its experimental realization and the ensuing beam dynamics.

The aim of this paper is to analyze the spatial, temporal and spectral pulse reshaping mechanisms leading to the experimentally observed SH phase transition [18]. We first show that the phase transition of the stationary states indeed exists in the experimental system featuring two SH modes interacting with the FW. However, in the experimental situation we find a highly nonstationary behavior still exhibiting the generic phase transition. The dynamics leading to the power dependent generation of staggered SH involves spatial focusing and generation of new frequency components.

#153927 - $15.00 USD Received 7 Sep 2011; revised 16 Oct 2011; accepted 20 Oct 2011; published 1 Nov 2011

In Sec. 2 we first introduce the experimental system under consideration and review the properties of the soliton phase transition with respect to this particular experimental case. In Sec. 3 we numerically calculate the beam propagation and analyze the reshaping mechanisms leading to the phase transition. We also identify the distinct features of the pulses, namely the generation of staggered SH in distinct wavelength regions, which are accessible for measurements. Our experimental findings are presented in Sec. 4 where we confirm our numerical results by spatio-spectral measurements probing the spatial and temporal spectrum of the SH. Finally we will present our conclusions in Sec. 5.

2. Spatial cw soliton phase transition with two SH modes

The experiments showing the soliton phase transition reported in [18] were conducted in periodically poled lithium niobate WGAs [28]. Fig. 1(a) shows the refractive index profile of these WGAs, which support only one FW mode at wavelengths around 1500 nm. The FW mode can interact nonlinearly with several SH modes via type I phasematching, where the interaction strength is controlled by the mode overlap and the wavelength dependent phase mismatch

$$\Delta\beta_j = 2k_U^0 - k_{V,W}^0 + \frac{2\pi}{\Lambda_{\mathrm{QPM}}}, \tag{1}$$

where Λ_{QPM} is the grating period and we consider the first-order QPM process only. The k_U^0 and $k_{V,W}^0$ are the propagation constants of the interacting FW and SH modes in the absence of linear coupling (corresponding to propagation in an isolated waveguide). The index j denotes the different nonlinear interactions. The most efficient interaction for a pair of SH and FW modes is achieved at wavelengths where the respective $\Delta\beta_j = 0$, which can be controlled by the quasi-phasematching period Λ_{QPM} and the device temperature. A main result in [18] is that the soliton phase transition is linked to the linear coupling of the participating SH mode to the neighboring

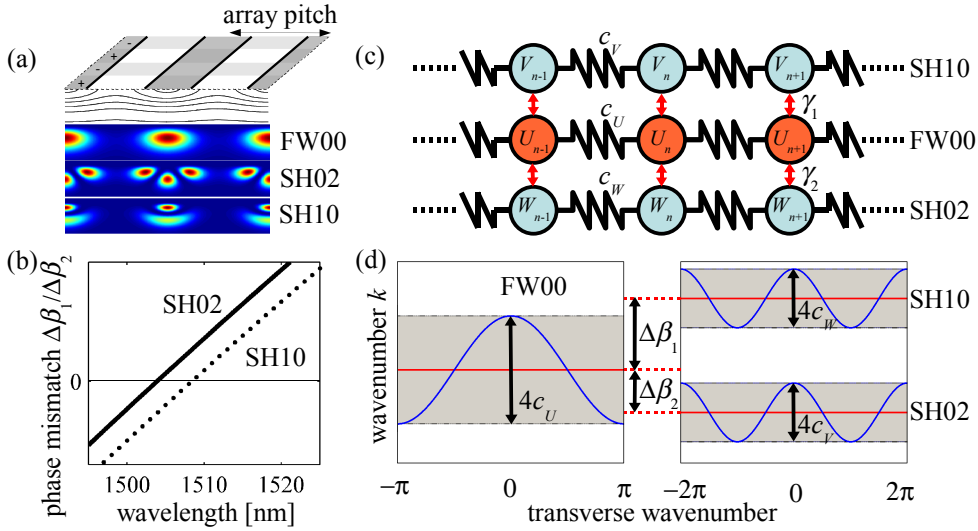

Fig. 1. (a) Sketch of the lithium niobate sample showing the refractive index profile [28], the periodic poling and the FW and SH modes. (b) Dependence of the mismatches between FW00 and SH02 (solid line) and SH10 (dotted) modes on the FW wavelength. (c) Scheme of the coupling mechanisms of the investigated system. (d) Scheme of the bands of FW (left) and SH (right).

#153927 - $15.00 USD Received 7 Sep 2011; revised 16 Oct 2011; accepted 20 Oct 2011; published 1 Nov 2011

waveguides and can not be observed if this linear coupling vanishes. Hence it is mandatory to use the SH02 mode depicted in Fig. 1(a), which features a linear coupling strength similar to the FW00 mode. In the used samples a quasi-phasematching period of $\Lambda_{\mathrm{QPM}} = 16.803\mu$m is employed to achieve efficient nonlinear interaction between FW00 and SH02 at an FW wavelength of approximately 1500 nm. We plot the simulated phase mismatch $\Delta\beta_1$ between the two modes vs. the FW wavelength in Fig. 1(b). However, in the same wavelength range the phase mismatch $\Delta\beta_2$ between FW00 and SH10 mode [see mode profile in Fig. 1(a)] becomes small [29, 30], leading to efficient nonlinear interaction. Hence in our analysis we have to consider a system featuring all the coupling mechanisms shown in Fig. 1(c). The amplitudes U_n, V_n and W_n of the FW00, SH02 and SH10 modes in the nth waveguide are coupled linearly with the coupling strengths c_U, c_V, c_W to the same modes in the neighboring waveguides. Additionally the FW component is coupled with the nonlinear coupling strengths γ_1 and γ_2 to the SH02 and SH10 modes at the same waveguide where the efficiency of the interaction is controlled by the phase mismatches $\Delta\beta_1$ and $\Delta\beta_2$. As can be seen in Fig. 1(b), the difference between the phase mismatches is constant with $\Delta\beta_1 - \Delta\beta_2 = 5\pi/\mathrm{cm}$. The linear propagation of the waves in the WGA is determined by the dependence of the longitudinal wavenumber k_m on the transverse wavenumber κ_m and the propagation constant of the single waveguide k_m^0. In the case of small coupling strengths this dispersion relation can be expressed analytically as

$$k_m = k_m^0 + 2c_m \cos(\kappa_m), \tag{2}$$

where the index $m = \{U, V, W\}$ again denotes the band, and the κ_m are normalized to the array pitch. Fig. 1(d) shows a scheme of the three bands governing the propagation of the modes taken into account here.

The nonlinear propagation of cw-waves in the lithium niobate WGA, taking into account one FW and two SH modes, can be described with the following coupled mode equations for the mode amplitudes in the waveguides [29, 31]:

$$\begin{aligned} i\frac{dU_n}{dz} + c_U(U_{n+1} + U_{n-1}) + \omega_U(\gamma_1 V_n + \gamma_2 W_n)U_n^* &= 0 \\ i\frac{dV_n}{dz} + c_V(V_{n+1} + V_{n-1}) - \Delta\beta_1 V_n + \omega_U \gamma_1 U_n^2 &= 0 \\ i\frac{dW_n}{dz} + c_W(W_{n+1} + W_{n-1}) - \Delta\beta_2 W_n + \omega_U \gamma_2 U_n^2 &= 0. \end{aligned} \tag{3}$$

Here z is the propagation distance and ω_U the mean frequency of the FW wave. The physical coupling constants of the used sample are $c_U = c_V = 80/\mathrm{m}$ and $c_W = 16/\mathrm{m}$. These coupling constants are used for the theoretical analysis as well and are considered constant in the investigated wavelength range around an FW wavelength of 1500 nm. The power $P = \sum_n \left(|U_n|^2 + |V_n|^2 + |W_n|^2\right)$ is conserved during the propagation. Similar to [18] we use the ansatz $U_n(z) = U_n^0 \exp(i\beta z)$, $V_n(z) = V_n^0 \exp(2i\beta z)$, $W_n(z) = W_n^0 \exp(2i\beta z)$ to calculate numerically the stationary solutions of Eqs. (3). Due to nonlinear synchronization, the propagation constant of the stationary solutions is defined for all components by β. This ansatz is plugged into Eqs. 3 and the ensuing system of nonlinear equations is solved numerically for propagation constants $\beta < 0$ where the stationary solutions show the phase transition [18].

As it is well known from spatial solitons with only one SH component, the FW part of solutions with $\beta < 0$ has phase jumps of π between adjacent waveguides (staggered phase profile) [32]. This is equivalent to a concentration of the FW energy at transverse wavenumbers of $\kappa_U = \pm\pi$ in the periodic spatial spectrum. However, [18] showed that a linearly coupled SH component switches it's phase profile at a certain propagation constant from unstaggered to

#153927 - $15.00 USD Received 7 Sep 2011; revised 16 Oct 2011; accepted 20 Oct 2011; published 1 Nov 2011

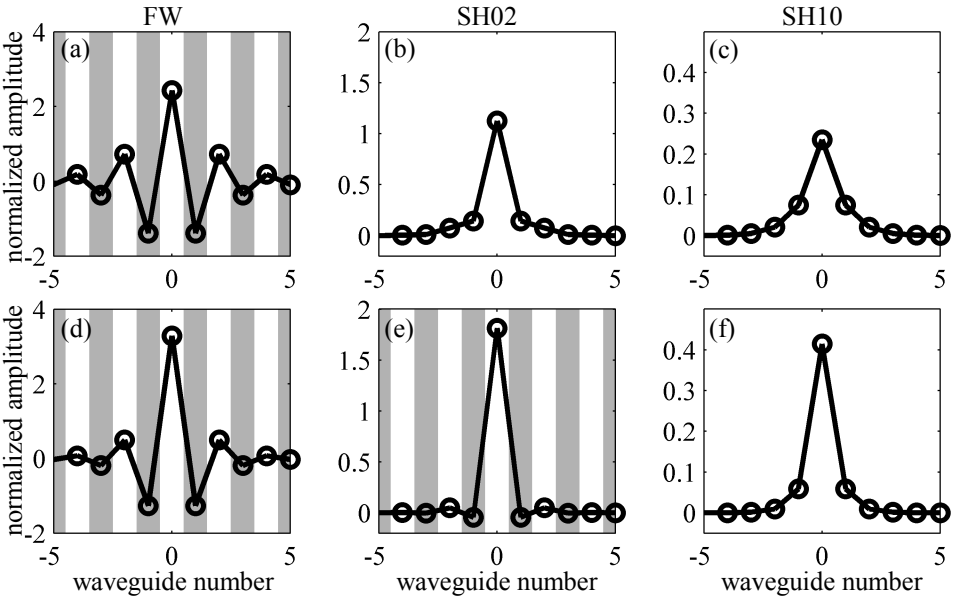

Fig. 2. Soliton solutions with (a,d) FW/U_n, (b,e) SH02/V_n, and (c,f) SH10/W_n components. For all plots, the mismatch is $\Delta\beta_1 = 0$ and the propagation constants are (a,b,c) $\beta = -200/\mathrm{m}$ and (d,e,f) $\beta = -240/\mathrm{m}$. The circles show the mode amplitudes and the shading denotes the phase where white corresponds to a phase of 0 and gray to a phase of π. The lines connecting the amplitude values are guides to the eye.

staggered. This phase transition of the topology is attributed to the narrowing of the localized solutions with increasing magnitude of β. In Fig. 2 we plot mode amplitudes and phases of two solutions which are just below and above this threshold propagation constant for the transition in the SH02 component. As expected, the FW component [Figs. 2(a,d)] is staggered for both solutions. However, the width of the FW component is slightly smaller for the solution with higher magnitude of the propagation constant. This small change in the width is enough to trigger the phase transition in the SH02 component, as can be seen in Fig. 2(e). For $\beta = -200/\mathrm{m}$ the SH02 amplitudes are not staggered because of the broader FW component. For $\beta = -240/\mathrm{m}$ the FW is narrow enough to allow for the staggered SH02. However, the SH10 component, depicted in Figs. 2(c,f) is not staggered for both propagation constants due to its smaller linear coupling constant. For much larger magnitude of β the SH10 component will also undergo the phase transition (not plotted). Similar result for localized solutions have been obtained in Ref. [33] where the authors use a continuous ansatz to describe periodic nonlinear systems with several bands. However, the obtained discrete-type equation and solutions accounted for only one SH mode.

To summarize this section, we showed that the theoretical results of [18] are still valid in a system with two SH modes, which corresponds to our experimental case. We found that there exist separate threshold propagation constants for all participating SH modes, depending on their linear coupling constants. In the next section we will investigate numerically the effects of pulsed signals in the generation of staggered SH components.

#153927 - $15.00 USD Received 7 Sep 2011; revised 16 Oct 2011; accepted 20 Oct 2011; published 1 Nov 2011

3. Pulse dynamics near the phase transition: numerical studies

Pulsed beams have a finite spectral width, hence we have to take the dispersive characteristics of the propagating modes of the WGAs into account. Accordingly we use the following coupled mode equations similar to Eqs. (3), but with additional terms accounting for temporal dynamics:

$$\begin{aligned} i\frac{dU_n}{dz} - \frac{D_U}{2}\frac{\partial^2 U_n}{\partial\tau^2} + c_U(U_{n+1}+U_{n-1}) + \omega_U(\gamma_1 V_n + \gamma_2 W_n)U_n^* &= 0 \qquad (4)\\ i\frac{dV_n}{dz} - \frac{D_V}{2}\frac{\partial^2 V_n}{\partial\tau^2} + i\delta_V\frac{\partial V_n}{\partial\tau} + c_V(V_{n+1}+V_{n-1}) - \Delta\beta_1 V_n + \omega_U\gamma_1 U_n^2 &= 0\\ i\frac{dW_n}{dz} - \frac{D_W}{2}\frac{\partial^2 W_n}{\partial\tau^2} + i\delta_W\frac{\partial W_n}{\partial\tau} + c_W(W_{n+1}+W_{n-1}) - \Delta\beta_2 W_n + \omega_U\gamma_2 U_n^2 &= 0. \end{aligned}$$

Here τ is the time relative to the frame moving with the FW group velocity. The parameters δ_V and δ_W are the differences in the inverse group velocities between the FW mode and the SH02 and SH10 modes, respectively. Finally, D_m accounts for the group velocity dispersion of the mode labeled by the index m. Eqs. (4) can be integrated numerically by using the standard split-step-algorithm [34]. We account for dispersion only up to the second order, because the shortest temporal features which we observe in our simulations (presented below) have a length of about 2 ps. However, for much shorter pulses, higher order dispersion may play an important role [35].

First we analyze the power dependence of the output of the WGA. Similar to the experiment discussed in Sec. 4 below, we launch an FW pulse with Gaussian shape in space and time and a temporal (spatial) full-width half-maximum (FWHM) width of 5.3 ps (4 waveguides).

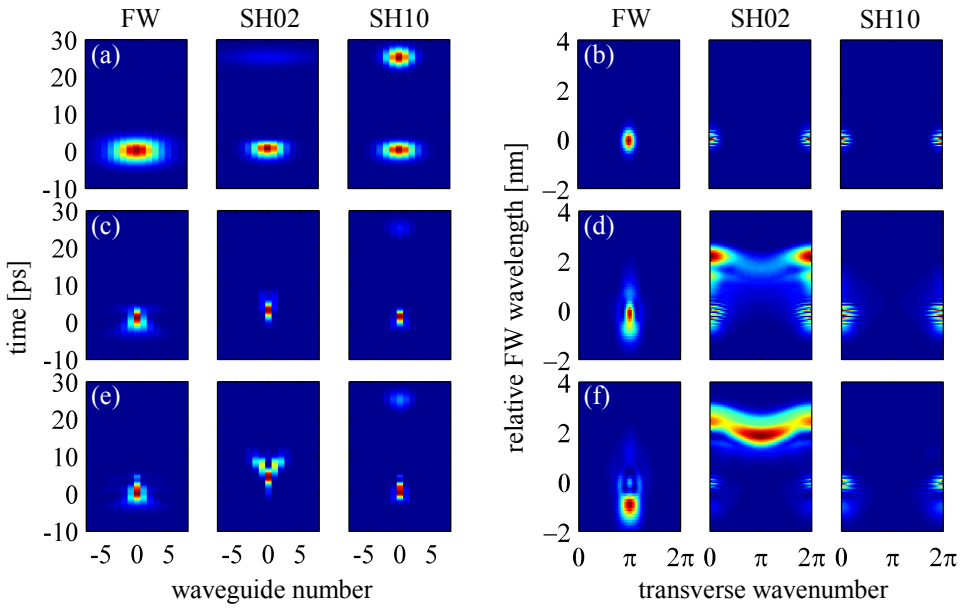

Fig. 3. Numeric simulations of the output intensities after 71 mm propagation for (a,b) 2 kW, (c,d) 5 kW,and (e,f) 7.0 kW FW input peak power for $\Delta\beta_1 = -4\pi/\text{cm}$. (a,c,e) show the intensities in real space and (b,d,f) show the spatio-temporal spectra for the FW (left), SH02 (center) and SH10 (right). Media 1 shows the array output intensities for a continuous scan of the input power.

#153927 - $15.00 USD Received 7 Sep 2011; revised 16 Oct 2011; accepted 20 Oct 2011; published 1 Nov 2011

The mismatch is set to $\Delta\beta_1 = -4\pi/\mathrm{cm}$, corresponding to an FW wavelength 2.2 nm below the FW00-SH02 phasematching wavelength. A phase difference of π is introduced between adjacent waveguides to fulfill the conditions found for the FW part of the stationary solutions. The output of the WGA after 71 mm of propagation for three different powers is plotted in Fig. 3 (Media 1), where the amplitude in each panel is normalized to the respective maximum. Fig. 3(a,b) for an input peak power of 2 kW correspond to the realization of a wide spatial soliton similar to [15]. Here the spatial width of the FW pulse after 71 mm of propagation is the same as the input beam width. The pulses of the two SH components, as seen in Fig. 3(a) are temporally split in two parts, one which travels with the group velocity of the SH and one which is trapped with the FW pulse [36–38]. The spatio-temporal spectra, plotted in Figs. 3(b), show that the FW part is localized at transverse wavenumbers of π corresponding to a staggered wave. However, due to the large spatial width of the FW field the SH is unstaggered and concentrated at transverse wavenumbers of 0 and 2π. The wavelength scale of the SH components is given in units of the corresponding FW wavelength.

For an input peak power of 5 kW the output of all three components is focused to almost only one waveguide [see Fig. 3(c)]. Since the power, and therefore the nonlinear phase shift, is weaker at the leading and trailing edges of the FW pulse, the focusing is not so pronounced there. We note that this effect was used in WGAs with Kerr-nonlinearity to excite X-waves [20]. The FW spectrum, shown in Fig. 3(d), is broadened due to effective self-phase modulation. However, the broadening is not symmetric since the cascaded phase shifts depend on the wavelength and the FW power shifted to longer wavelengths comes very close to the phasematching wavelength of the FW00 and SH02 modes at a relative wavelength of 2.2 nm. Hence it is very effectively transformed into SH. This can be seen in the spatio-temporal spectrum of the SH02 component, where the maximum power is now located at the phasematching wavelength 2.2 nm above the input FW wavelength. Due to the decreased spatial width of the FW, the SH is now generated for a broad spectrum of transverse wavenumbers, however the SH02 wave is still unstaggered at the beam center.

Finally we plot results for an input peak power of 7 kW in Fig. 3(e) and (f). The FW pulse is again strongly localized and the X-shape is maintained. But whereas the SH10 component still travels mainly with the FW pulse, the SH02 wave radiates away from the FW pulse and diffracts. This is a consequence of the very efficient SHG at the phasematching wavelength. The SH can be kept under the envelope of the FW pulse if it is constantly generated and annihilated by the cascading process. However, the large amplitude SH02 is phase-matched and traveling with the same speed as the generating FW wave. Hence it is not subjected to cascading and propagates with the SH group velocity. Since the SH02 component also couples linearly to adjacent waveguides the SH pulse consequently diffracts. Even though the SH02 is definitely not part of a stationary state we see in Fig. 3(f) that now staggered SH is generated and the maximum of the SH02 component is at transverse wavenumbers of $\kappa_1 = \pi$. However, the staggered SH is only generated at the phasematching wavelength of the FW and the SH02 component. This also leads to the strong asymmetry of the FW spectrum. As can be seen for all simulated powers, the SH10 does not participate in the generation of staggered SH. This is due to the larger mismatch and weaker linear inter-waveguide coupling of the SH10, which leads to its much higher threshold power for the phase transition [18]. For that reason we will not present the results for the SH10 wave in our analysis of the propagation in the sample. However, the SH10 component enhances the focusing of the FW wave by providing additional phase shifts. This leads to a much smaller threshold power for the generation of the staggered SH02 as we verified by integrating Eqs. (4) with the same input parameters as used up to now and $\gamma_2 = 0$.

After we identified a power level where staggered SH is generated at the SH02 component we will explore how this process takes place during the propagation inside the array. Our sim-

#153927 - $15.00 USD Received 7 Sep 2011; revised 16 Oct 2011; accepted 20 Oct 2011; published 1 Nov 2011

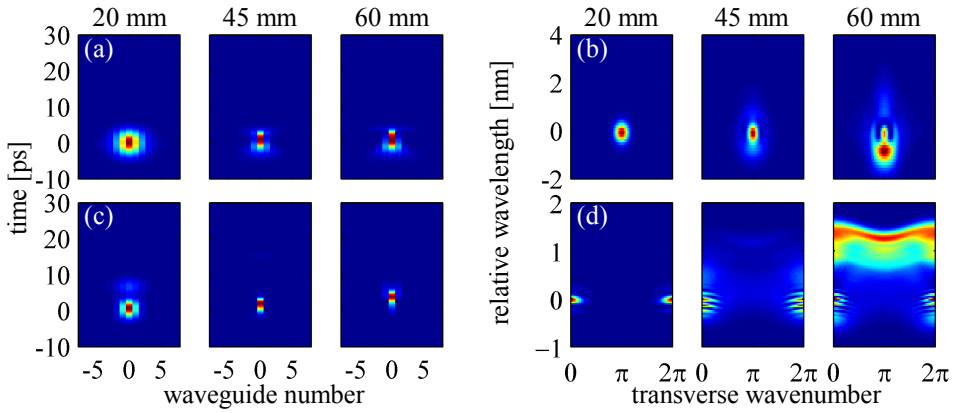

Fig. 4. (a,b) FW and (c,d) SH02 intensities after different propagation lengths for an FW input peak power of 7 kW and $\Delta\beta_1 = -4\pi/\text{cm}$. (a,c) intensities in real space and (b,d) spatio-temporal spectra after 20 mm (left), 45 mm (middle), and 60 mm propagation. The propagation through the sample in steps of 1 mm is also presented in Media 2.

ulations of Eqs. (4) show that for higher powers no spatial soliton is generated. To explore the propagation dynamics we use the same initial parameters as above for an FW input peak power of 7 kW and plot the FW and SH02 intensities after different propagation lengths in Fig. 4 (Media 2). We find that initially the FW and the generated SH02 are narrowing. After 20 mm of propagation the trailing pulse of the SH not retained under the FW pulse is clearly visible. After 45 mm the pulses, especially the SH, are focused to only one waveguide. The FW spectrum [Fig. 4(b)] is broadened and although the asymmetry in the FW spectrum is not visible the onset of the generation of staggered SH02 can be seen in Fig. 4(d) at the relative SH wavelength 1.1 nm. After 60 mm the maximum of the space-time SH intensity is moving towards the tail of the FW pulse and the onset of diffraction is visible in Fig. 4(c). Additionally, the tail of the FW pulse is now focused very strongly. Here the conditions for the generation of staggered SH states are met and the pulse locally has a similar profile as the calculated stationary solutions. Hence the SH02 component is primarily generated at transverse wavenumbers of π. This happens with the largest efficiency at the phasematching wavelength, leading to the asymmetric shape in the FW spectrum. However, due to the strong localization of the FW, SH intensity is generated for a large range of transverse wavenumbers. Since the phasematching condition is only fulfilled for one longitudinal wavenumber, the SH is generated along isolines of it's dispersion relation. For the SH these isolines follow a cosine as defined in Eq. (2). SH states existing at the isolines of the dispersion relation were referred to as SH X-waves in [24,26]. In [24] also the SH radiation cone which is supported in it's origin by the FW is predicted, exactly as we find it after the last 10 mm of propagation [Fig. 3(e)].

To conclude the section on our simulations, we found that staggered SH is indeed generated with pulsed excitation of the FW wave only. However, the staggered SH is the result of complex FW and SH pulse transformations including focusing, frequency shifts and the generation of X-waves. We do not find a spatio-temporal soliton with staggered SH component but confirm that the phase transition is a generic effect in nonlinear propagation with linearly coupled SH waves. In the following we will experimentally prove the results of the simulations by measuring the characteristic spectral features at the output of our a WGA.

#153927 - $15.00 USD Received 7 Sep 2011; revised 16 Oct 2011; accepted 20 Oct 2011; published 1 Nov 2011

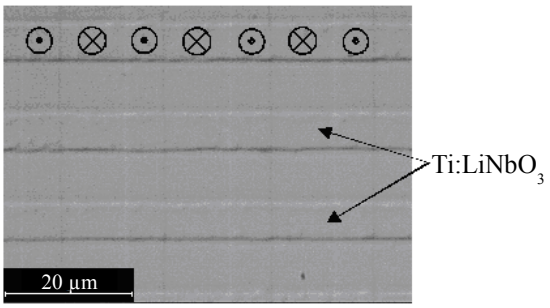

Fig. 5. Microscope image of the used sample showing the titanium indiffused waveguides and, indicated by the up- and downward arrow signs, the poling pattern.

4. Experimental measurements

Measurements were performed in a 71 mm long array of waveguides in periodically poled lithium niobate consisting of 101 waveguides. The waveguides were fabricated by indiffusion of titanium stripes of 101 nm thickness and 7μm width for 8.5 h at a temperature of 1060 °C [28]. A microscope image of the sample we use in our experiments is shown in Fig. 5. The array period of 15μm results in linear coupling strengths of $c_U = c_V = 80/\mathrm{m}$ for the FW and SH02 modes and $c_W = 16/\mathrm{m}$ for the SH10 mode. The FW coupling constants are obtained by measuring the Green's function of the waveguide arrays [12] whereas we calculate the SH bands with a freely available software package [39] to determine the SH coupling constants. The given values have been used already for the calculation of the stationary solutions and in the simulations in Sec. 2 and Sec. 3 above. To perform our experiments TM-polarized light from an optical paramatric amplifier is shaped by an elliptical telescope and the resulting focus of a horizontal (vertical) FWHM of 60 (3) μm is imaged on the front facet of the sample. To achieve the necessary phase difference of π between adjacent waveguides the input beam is tilted by off-axis illumination of the coupling objective. This results in an excitation of the waveguides with a spatial FWHM of 4 waveguides. However, not only the FW00 mode but also the 2nd FW mode FW01 is weakly excited. The FWHM length of the pulses is 5.3 ps and the amplifier provides peak powers up to $\approx$ 12kW with a repetition rate of 5 kHz. To prevent photorefraction by the generated SH radiation the sample is heated to a temperature of 220 °C. At this sample temperature the experimentally used FW wavelength of 1499 nm corresponds to a mismatch between FW00 and SH02 mode of $\Delta\beta_1 = -4\pi/\mathrm{cm}$. This is the same mismatch as used for the simulations in Sec.3. To measure the output of the WGA we simultaneously image the output facet onto an InGaAs- and a CCD-camera to record the spatial profiles of the FW and SH output. To obtain the spatial spectrum of the SH we employ an additional lens in a 2-f configuration to generate a Fourier transform of the SH output. This is recorded with an additional CCD-camera.

The power dependence of the time integrated outputs of the WGA measured with this setup is plotted in Fig. 6 for powers from 1 kW to 10 kW. At the lowest shown power the FW component [see Fig. 6(a)] is already narrower than a linear diffracted beam. For increasing power the spatial width further decreases until the maximal focusing is reached at an input peak power of 2 kW. However, in contrast to the simulations the FW is not focused to only one waveguide. Instead the width of the FW beam at 2 kW corresponds to the width of the coupled input distribution. Hence at this power we excite a wide spatial soliton, in agreement with [40] and Fig. 3(a). For even higher power the FW beam broadens again. The width of the SH component in Fig. 6(b) is minimal at a power of approximately 6 kW which is in accordance with the sim-

#153927 - $15.00 USD Received 7 Sep 2011; revised 16 Oct 2011; accepted 20 Oct 2011; published 1 Nov 2011

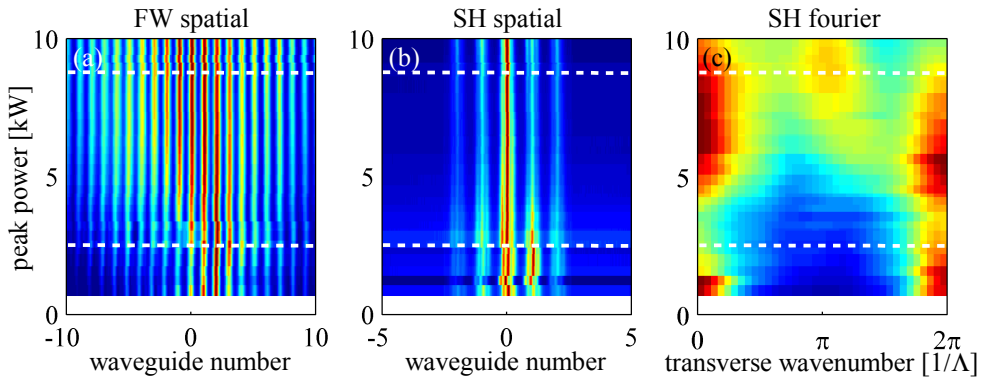

Fig. 6. Power dependence of the time integrated spatial intensity profiles at the array output. (a) FW and (b) combined SH intensities vs. power for an FW input wavelength of 1499 nm corresponding to a mismatch of $\Delta\beta_1 = -4\pi/\text{cm}$. (c) Corresponding power dependence of the SH spatial Fourier spectrum. The white dotted lines mark the power levels where spectrally resolved measurements are conducted.

ulation results. This corresponds to the power where staggered SH is measured at a transverse wavenumber of π [see Fig. 6(c)]. The discrepancies between simulation and measurement may be induced by the waveguide inhomogeneities and the SH induced photorefractive effects. We also note that the rectangular QPM grating [visible in Fig. 5] can fascilitate higher-order cascaded interactions which can act as effective cubic nonlinearity [41] in addition to first-order quadratic cascading interaction considered in the derivation of Eqs. (3) [see also Eq. (1)]. The effective cubic nonlinearity can significantly affect the FW beam dynamics for vanishing phase mismatch [42]. Hence the spectral components of the FW close to phase-matching, which are subject to the effective cubic nonlinearities, can be one of the reasons for the deviations of the measurement results from the simulations. We performed additional numerical simulations to fully accound for QPM-induced features and found that effective higher-order effects are very sensitive to QPM inhomogeneities and to the boundary conditions, i.e. the relative length of the first QPM period, and these preliminary results call for a separate study of QPM effects in waveguide arrays which is beyond the scope of this manuscript.

As was reported in [18] the power threshold for the generation of staggered SH predicted by

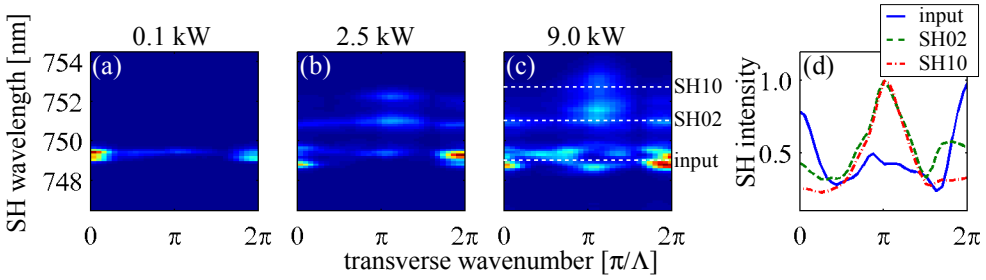

Fig. 7. Experimentally measured spectrally resolved spatial SH Fourier spectra for an FW input wavelength of 1499 nm ($\Delta\beta_1 = -4\pi/\text{cm}$) and an FW input power of (a) 0.1 kW, (b) 2.5 kW, and (c) 9 kW. (d) SH spatial spectrum for the wavelengths 749.5 nm (blue solid line), 751 nm (green dashed) and 752.8 nm (red dash-dotted) at a power of 9 kW. The dotted lines in (c) correspond to the wavelengths plotted in (d) according to the labels.

#153927 - $15.00 USD Received 7 Sep 2011; revised 16 Oct 2011; accepted 20 Oct 2011; published 1 Nov 2011

the simulation is confirmed by the time integrated measurements. However, to prove the spatio-temporal mechanism for the generation of staggered SH the integrated measurements are not sufficient. Due to the integration the information on the spectral structure of the generated staggered SH is lost. The unique feature of the generation mechanism is that staggered SH is not generated at a wavelength corresponding to the input FW but at the phasematching wavelength between FW00 and SH02. To show this experimentally we replace the CCD camera measuring the SH spatial spectrum by an imaging spectrograph. This enables us to measure a wavelength resolved spatial SH spectrum for a fixed input peak power. Results for three different peak powers are shown in Fig. 7(a-c). For a peak power of 0.1 kW the SH is generated exclusively at 749.5 nm which corresponds to our input FW wavelength of 1499 nm. The maximum of the SH intensity is localized at transverse wavenumbers of 0 and 2π, no staggered SH is generated during the propagation. Fig. 7(b) shows results for an input peak power of 2.5 kW, which is slightly larger than power of strongest focusing of the FW component [see Fig. 6(a)]. Here SH is not only detected at 749.5 nm but also at wavelengths of approximately 750.8 nm and 752.3 nm. These wavelengths are ≈ 0.5nm larger than the expected phasematching wavelengths to the SH02 and SH10 modes which we measured independently with a low power cw FW input beam. However, it was shown before in a single waveguide that, due to cascading, the phasematching wavelengths shift to higher wavelengths with increasing input power [29]. Hence this SH power can be attributed to phasematching to the two SH modes. Although we did not detect staggered SH in the time integrated measurements for this input power, the maximum of the SH generated at the phasematching wavelengths is clearly at transverse wavenumbers of π for both SH modes. The power of the staggered components is just too weak to be detected in the integrated measurements shown above. Finally we show a measurement result for a power of 9 kW in Fig. 7(c). Here we now see strong staggered SH components generated at both SH modes, where the maxima are shifted further towards longer wavelengths. To emphasize that the main contribution to the staggered SH indeed is generated at the phasematching wavelengths we integrate the SH intensity of Fig. 7(c) over spectral domains centered at the (shifted) phasematching wavelengths with a spectral width corresponding to the spectral width of the input pulse. The central wavelengths are indicated by the dotted white lines in Fig. 7(c). The normalized result is plotted in Fig. 7(d). It shows that the SH intensity maximum at the phasematching wavelengths of 751 nm for the SH20 and 752.3 nm for the SH10 is at a wavenumber of π. In contrast, the maximum intensity is at $0, 2\pi$ for the SH generated at 749.5 nm, corresponding to half of the input FW wavelength.

The results shown in Fig. 7 support the conclusions drawn from the numerical simulations by confirming the key mechanism of staggered SH generation. It is only generated after the FW focusing takes place and the staggered components stem from spectral components at the phasematching wavelengths. However, our measurements also show some differences. Most notably, a weak staggered SH appears at lower powers than in the simulations which was not detectable in the time integrated measurements.

This difference can be explained by the action of other FW-SH interactions not taken into account in the simulations. A spectrum of the SH output integrated over all transverse wavenumbers, shown on Fig. 8, suggests that SH is also generated at the phasematching wavelengths of the FW00 mode with the SH00 mode (778 nm). Additionally we excite the higher order FW01 mode and we detect SH power at 746 nm which may be explained by phasematching of the FW00 and FW01 modes to the SH11 mode. All these interactions will create additional phase shifts not accounted for in the simulations which will influence the power threshold of the dynamic phase transition.

Another feature measured in the experiment is that not only the SH02 takes part in the phase transition like in the simulations but also spectral components at the FW00-SH10 phasematch-

#153927 - $15.00 USD Received 7 Sep 2011; revised 16 Oct 2011; accepted 20 Oct 2011; published 1 Nov 2011

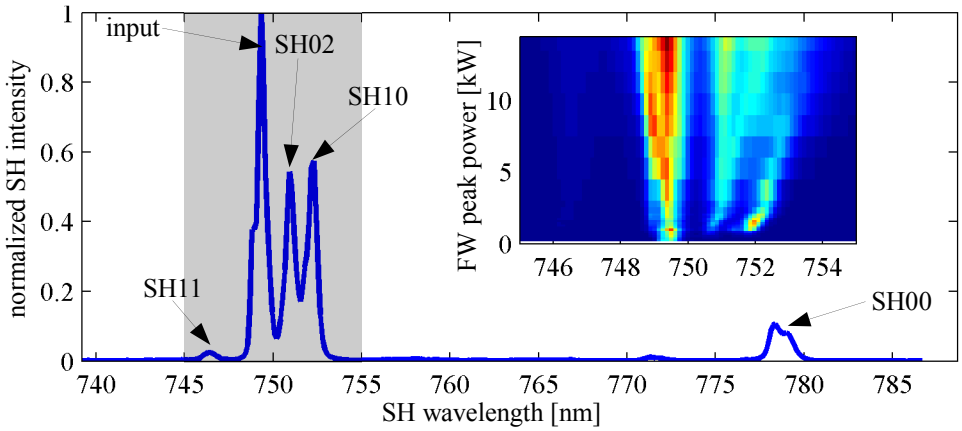

Fig. 8. SH output spectrum for an FW input wavelength of 1499 nm ($\Delta\beta_1 = -4\pi/\mathrm{cm}$) and an input peak power of 2.5 kW. The labels denote maxima in the spectrum corresponding to phasematching with the indicated SH modes. The inset shows the power dependence of the spectral band indicated by the gray background.

ing wavelength are staggered. This may be a sign that the coupled mode equations, which are valid for weakly coupled independent bands, have certain limitations for the description of our system due to interactions between the SH bands, leading to changes in the cosine-shape of the bands. We calculated the SH bandstructures using the plane-wave-expansion method with the simulated profile of the index of refraction of the WGA and found no evidence for a failure of the model. However, at higher power the bands may be deformed, leading to the shift of the phasematching wavelengths shown in the inset of Fig. 8. At 2 kW input power the phasemaching wavelengths are already significantly shifted, hence potential band deformations already affect the nonlinear interactions. This may explain the measurement in Fig. 7(b) showing staggered SH at the SH10 mode already at 2.5 kW input power.

5. Conclusion

We investigated, both theoretically and experimentally, the influence of the temporal and spectral extent of pulsed beams on the topological soliton phase transition reported in [18]. Particularly we analyzed the influence of the existence of two SH components and especially the impact of pulsed excitation with FW light only. First we show that the phase transition still takes place in the stationary localized solutions of the system with two SH components. We found different threshold propagation constants for the two SH components, due to different linear coupling and mismatches. This was confirmed by simulations of pulsed propagation, where we found that only the SH02 mode plays a role in the generation of staggered SH components. Indeed the transition from unstaggered to staggered SH output happens for the strongest spatial focusing of all waves as was found in [18]. However, the simulations revealed that no stationary states are excited. Conversely, the generation of pulsed staggered SH is a highly non-stationary process involving spatial focusing and frequency shifts. We find that staggered SH02 components are generated exclusively at the phasematching wavelength between FW00 and SH02 modes, independent from the FW input wavelength. The FW is first shifted in wavelength by cascaded self-phase modulation and then efficiently transferred to SH. The resulting staggered SH pulse resembles an SH X-wave [24].

This mechanism was proved also experimentally by measurements resolving both the tempo-

#153927 - $15.00 USD Received 7 Sep 2011; revised 16 Oct 2011; accepted 20 Oct 2011; published 1 Nov 2011

ral and spatial spectrum of the SH output of a lithium niobate WGA. We find that staggered SH is generated at the phasematching wavelengths to the SH modes only. However, in contrast to the simulation, both SH02 and SH10 modes contribute to the generation of staggered SH. This is attributed to nonlinear interactions with other modes not taken into account in the simulations and to changes in the properties of the bands of the WGA due to strong nonlinear interactions.

Acknowledgments

The authors acknowledge support by the Australian Academy of Science and the International Bureau of the Federal Ministry of Education and Research in Germany under the Australia-Germany Researcher Mobility Call 2010-2011, the Go8-DAAD (Australia-Germany Joint Research Co-operation Scheme), the German Research Foundation (NanoGuide), the Federal Ministry of Education and Research (PhoNa), and the Thuringian Ministry of Education, Science and Culture (MeMa).

#153927 - $15.00 USD Received 7 Sep 2011; revised 16 Oct 2011; accepted 20 Oct 2011; published 1 Nov 2011